energies

MDPI

Article

Mixed-Lignin Precursor Engineering for Hierarchically Porous Pseudo-Graphitic Carbon Toward High-Performance Supercapacitors

Chenhao Sun, Zhongyang Luo *, Shurong Wang and Chunjiang Yu

State Key Laboratory of Clean Energy Utilization, Zhejiang University, 38 Zheda Road, Hangzhou 310027, China; chenhaosun@zju.edu.cn (C.S.); srwang@zju.edu.cn (S.W.); chunjiang@zju.edu.cn (C.Y.)
* Correspondence: zyluo@zju.edu.cn; Tel.: +86-571-8795-2440

Abstract

Developing biomass-derived carbon electrodes with simultaneously optimized pore architecture, graphitic ordering, and surface chemistry remains a challenge for high-performance supercapacitors. Herein, a dual-lignin precursor engineering strategy based on lignosulfonate and alkaline lignin is proposed to construct hierarchically porous carbons via an ex situ method. Benefiting from the complementary characteristics and cooperative interactions of the two lignins, the optimized carbon exhibits a well-balanced porous architecture composed of interconnected carbon nanosheets with predominantly pseudo-graphitic domains accompanied by locally graphitized regions. The mixed-lignin strategy effectively regulates sulfur retention and removal during carbonization, while the coexistence of oxygen- and sulfur-containing functional groups may improve electrode wettability and contribute to charge storage, thereby favoring substantial outer-surface charge accessibility with contributions from other charge-storage processes. Among all samples, the optimized 2L1A electrode delivers a high specific capacitance of 386.7 F g^{-1} at 1 A g^{-1} in a three-electrode configuration. The assembled symmetric supercapacitor delivers an energy density of 40.4 Wh kg^{-1} together with 97.4% capacitance retention after 10,000 charge–discharge cycles. Comprehensive kinetic analyses further demonstrate rapid electron/ion transport, predominant surface-controlled charge storage, and excellent reversibility. This work demonstrates the potential of mixed-lignin precursor engineering for the rational design of high-performance carbon electrodes for advanced supercapacitors.

Keywords: lignin; precursor; hierarchically porous carbon; graphitization; sulfur regulation; electrochemical performance; supercapacitor

Check for updates

Academic Editor: Federico Barrero

Received: 2 September 2026
Revised: 12 October 2026
Accepted: 13 October 2026
Published: 16 October 2026

Copyright: © 2026 by the authors. Licensee MDPI, Basel, Switzerland. This article is an open access article distributed under the terms and conditions of the Creative Commons Attribution (CC BY) license.

1. Introduction

Electrochemical energy-storage technologies with rapid response, high power output, and long-term durability are becoming increasingly important for portable electronics, hybrid electric vehicles, and renewable-energy systems [1]. Among them, supercapacitors have attracted widespread interest because they can deliver high power density, fast charge–discharge rates, and excellent cycling stability [2]. Since the energy-storage behavior of supercapacitors is fundamentally determined by electrode materials, considerable efforts have been devoted to developing high-performance electrodes based on transition metal oxides, conducting polymers, and carbon materials [3]. Carbon-based electrodes remain particularly competitive because they simultaneously provide high electrical conductivity,

excellent chemical stability, and flexible control over pore structures [4]. Renewable biomass has therefore become an attractive carbon source, offering low cost together with abundant intrinsic surface functionalities [5]. As one of the most abundant aromatic biopolymers, lignin possesses a high carbon yield and abundant oxygen-containing functionalities, making it an ideal precursor for constructing functional porous carbon electrodes [6].

Lignin is generated in enormous quantities by the pulping industry, with an annual production exceeding 70 million tons worldwide [7]. Among various technical lignins, sodium lignosulfonate (LS) and alkaline lignin (AL) are two of the most abundant and representative industrial by-products, both of which have been extensively utilized in thermochemical conversion processes and have demonstrated considerable potential for large-scale valorization [8,9]. In recent years, lignin-derived porous carbons have attracted increasing attention as electrode materials for supercapacitors. For example, Dong et al. fabricated porous carbon by crosslinking AL with resorcinol to construct a hydrogel precursor, followed by chemical activation. The obtained carbon possessed a high specific surface area (SSA) of 2117 m^2 g^{-1} and delivered 228 F g^{-1} in a three-electrode configuration [10]. Liang et al. prepared hierarchically porous carbon spheres from corn-stover-derived AL through a combined Zn-doping and $KHCO_3$-activation strategy. The assembled symmetric supercapacitor (SSC) achieved an energy density of 17.5 Wh kg^{-1} and maintained 91.82% of its initial capacitance after 5000 cycles [11]. These studies collectively demonstrate the considerable potential of lignin-derived carbons for supercapacitor applications. Nevertheless, achieving precise regulation of carbon structure and electrochemical functionality remains an important challenge for further improving the performance of lignin-based electrodes.

In recent years, multicomponent precursor engineering has emerged as an effective strategy for tailoring carbon structures and improving electrochemical performance. A three-dimensional interconnected carbon network was developed by Sun et al. through the boric-acid-assisted self-assembly of chitosan and LS, followed by KOH activation [12]. Owing to its SSA of 2700 m^2 g^{-1}, the obtained material achieved a specific capacitance (C_g) of 332 F g^{-1} at 1 A g^{-1}. Micropore-enriched porous carbon was obtained by Yuan et al. via blending chitosan and gelatin in an acetic acid solution with subsequent $KHCO_3$ activation [13]. The as-prepared electrode exhibited a C_g of 331 F g^{-1} at 1 A g^{-1} in 6 M KOH electrolyte. Despite these encouraging results, most reported hybrid precursor systems are constructed from chemically different biomass components, making it difficult to distinguish their individual contributions to carbonization and the resulting structural evolution. Mixed-lignin systems, by contrast, are inherently more suitable for precursor engineering because the different lignin fractions share similar aromatic frameworks while retaining distinct molecular architectures and functional-group distributions. Such structural compatibility may facilitate intermolecular interactions among lignin species, improving precursor homogeneity, suppressing aggregation, and maintaining structural integrity during thermal conversion [14,15]. At the same time, interactions between different lignins are expected to influence decomposition behavior, carbon framework evolution, heteroatom retention, and pore formation, thereby providing additional opportunities to regulate the structure of porous carbons. Despite these potential advantages, the synergistic effects arising from the co-pyrolysis of different technical lignins have not yet been systematically clarified, especially with respect to their influence on microstructure evolution and electrochemical performance.

In this work, a dual-lignin strategy based on LS and AL was proposed to develop advanced porous carbon electrodes for supercapacitor applications. Benefiting from their complementary molecular characteristics, LS was expected to improve the dispersion of AL, whereas the mildly alkaline environment introduced by AL could help stabilize the precursor system and alleviate the aggregation tendency of LS. In addition, intermolecular

interactions, potentially involving hydrogen bonding and π–π stacking, may contribute to the formation of a more uniform precursor network, which is favorable for maintaining structural integrity and facilitating a possible cooperative carbonization effect during pyrolysis. These combined effects may affect sulfur (S) retention and elimination, carbon framework evolution, and pore structure formation, thereby contributing to improved electrochemical performance. Comprehensive physicochemical characterizations were performed to elucidate the structural evolution of the dual-lignin-derived carbons and their structure–property relationships. The optimized sample exhibited a well-developed hierarchical porous structure together with relatively enhanced graphitic ordering, supporting efficient ion diffusion and charge transport [16]. As a result, the obtained porous carbon electrode delivered a high C_g of 386.7 F g^{-1} at 1 A g^{-1}, while the assembled SSC achieved an energy density above 40 Wh kg^{-1}. Electrochemical kinetic analyses further clarified the ion transport process, charge-transfer behavior, and capacitive contributions. This study provides a practical precursor-engineering strategy for utilizing synergistic interactions between technical lignins in the rational design of high-performance carbon-based electrodes.

2. Materials and Methods

2.1. Materials

LS and AL were supplied by Aladdin Chemical Reagent Co., Ltd. (Shanghai, China). Potassium hydroxide (KOH, 86%, analytical grade (AR)), hydrochloric acid (HCl, 37%, AR), and absolute ethanol were purchased from Sinopharm Chemical Reagent Co., Ltd. (Shanghai, China). Deionized water (DI) was used throughout all experimental procedures.

2.2. Preparation of Dual-Lignin Porous Carbons

Dual-lignin porous carbons: Prior to use, all lignins were oven-dried at 80 °C to a constant mass. In a typical procedure, 2 g of LS was dissolved in 40 mL of DI and stirred at 400 rpm for at least 20 min at room temperature. A predetermined amount of AL powder was then gradually added, followed by stirring for 2 h to obtain a uniform dispersion. The mixture was concentrated at 80 °C under stirring to form a viscous paste, transferred into a corundum boat, and dried at 80 °C for more than 12 h. The dried precursor was pyrolyzed in a fixed-bed tubular furnace under a continuous N_2 atmosphere at a flow rate of 200 sccm. The temperature was raised to 800 °C at a rate of 10 °C min^{-1}, held for 2 h, and then naturally cooled to room temperature. The resulting pyrolytic carbon (PC) was mixed with KOH at a mass ratio of 1:3 [7,12,17], dried at 80 °C for 12 h, and activated under the same heating conditions. After activation, the samples were dispersed in hot DI at a solid-to-liquid ratio of 1 g per 50 mL, followed by dropwise addition of 1 M HCl until no further gas evolution was observed. The suspension was then sealed and stirred at 60 °C for at least 1 h. After the initial vacuum filtration, the samples were further washed and filtered with DI 2–3 times until approximately neutral pH was reached, followed by drying at 110 °C.

Sample nomenclature: The samples were designated according to their precursor composition and preparation route. The final products obtained from LS/AL mixtures were denoted as xLyA, where x/y represents the initial LS:AL mass ratio. LSPC and ALPC denote the chars obtained by direct pyrolysis of LS and AL, respectively, without subsequent KOH activation. The dried precursor mixture with an LS:AL mass ratio of 2:1 was denoted as 2LS + 1AL, whereas the corresponding carbon obtained by pyrolysis without KOH activation was designated as 2L1A-N. L-K and A-K represent the samples obtained by pyrolysis and subsequent KOH activation of LS and AL, respectively. For comparison, LAK and 2LAK were prepared via in situ activation by directly mixing LS,

AL, and KOH at mass ratios of 1:1:3 and 2:1:4.5, respectively, under otherwise identical preparation conditions.

3. Results and Discussion

3.1. Preparation Optimization, Synergistic Carbonization, and Representative Sample Selection

As summarized in Table S1 (Supplementary Materials), the final carbon yield strongly depends on the preparation strategy. Among all samples, A-K and LAK give yields below 5%, making them unsuitable for practical production. Preliminary electrochemical evaluation further shows that LAK delivers a C_g of 317 F g^{-1} at 0.5 A g^{-1} (Figure S1b, Supplementary Materials), but only 37% of this value is retained when the current density increases to 10 A g^{-1}, reflecting unsatisfactory rate performance. In addition, the CV curve becomes noticeably distorted at high potentials (Figure S1a), indicating pronounced polarization during the charge-storage process [18]. Similarly, the CV curve of 2LAK exhibits more severe distortion (Figure S1c), while the maximum C_g obtained from the GCD curves is only 24 F g^{-1} (Figure S1d), which is far lower than that of LAK, indicating its very poor electrochemical performance. The ex situ and in situ activation routes differ in the stage of KOH introduction and the corresponding KOH-to-precursor mass ratios. These differences may influence the pore structure and surface properties of the resulting carbons, potentially affecting their carbon yields and electrochemical performance.

To investigate the reason for the low yield of A-K, the pyrolytic carbons derived from LS and AL (LSPC and ALPC) were analyzed by XRD (SmartLab SE, Rigaku, Tokyo, Japan) and Raman spectroscopy (LabRAM HR Evolution, Horiba, Kyoto, Japan) for comparison (Figure S2). LSPC shows a more distinguishable (002) diffraction peak, along with a lower I_D/I_G ratio and a more discernible 2D band, suggesting a higher degree of structural ordering and fewer defects. Such characteristics are beneficial for preserving carbon frameworks during KOH activation, thereby contributing to the relatively higher yield of L-K [17].

Notably, all ex situ activated lignin blends exhibit carbon yields approaching or exceeding 10%. This improvement may be associated with intermolecular interactions, such as hydrogen bonding and π–π stacking, between LS and AL, leading to the formation of more homogeneous precursor networks [12]. Consistently, a viscous gel-like phase is formed after thermal stirring (Figure S3), indicating enhanced compatibility between the two lignin components. Fourier transform infrared spectroscopy (FTIR) results (Figure S4) suggest possible intermolecular interactions between LS and AL. The O–H stretching band shifted from 3422 and 3420 cm^{-1} for LS and AL to 3409 cm^{-1} for 2LS + 1AL, indicating strengthened intermolecular interactions, possibly associated with hydrogen bonding between the lignin components [19]. The aromatic skeleton vibration shifted from 1607 cm^{-1} for LS and 1576 cm^{-1} for AL to 1595 cm^{-1} for 2LS + 1AL, suggesting a modified aromatic environment, potentially involving π–π stacking between LS and AL [20,21]. In addition, the characteristic bands around 1122–1136 cm^{-1} observed for LS and AL, assigned to aromatic C–H in-plane deformation [22], were replaced by a new band at 1205 cm^{-1} in 2LS + 1AL, which is associated with C–O/C–C-related vibrations and further indicates a changed chemical environment upon mixing [23,24]. The thermogravimetric analysis (TGA) and derivative thermogravimetry (DTG) results further reveal deviations from the theoretical additive behavior during the thermal conversion of the lignin blends (Figure S5). The thermal decomposition can be broadly divided into three stages, corresponding to internal water removal, the main pre-carbonization decomposition (150–660 °C), and high-temperature devolatilization and carbonization (660–800 °C), respectively. Notably, 2LS + 1AL exhibits clear deviations from its theoretical additive profile, with mass differences of 1.8%, 4.4%, and 2.2% at 800 °C, the maximum deviation point, and after the isothermal holding period, respectively (Figure S5a,c). These non-additive mass-loss behaviors indicate that LS

and AL undergo altered thermal conversion when mixed. Moreover, the two major DTG peaks appear earlier for 2LS + 1AL, decreasing from 273.2 and 769.5 °C for the theoretical profile to 230.9 and 759.8 °C, respectively, accompanied by pronounced changes in the corresponding mass-loss rates (Figure S5b). This suggests that mixing LS and AL may lower the temperature required for thermal conversion and carbonization. Together with the FTIR results, these deviations suggest possible cooperative interactions and carbonization between LS and AL. As shown in Table S1, carbon yield increases with increasing LS content and reaches a maximum at LS/AL ratios of 2:1–3:1. In summary, LAK, 2LAK and A-K are not considered in subsequent investigations owing to their low carbon yields and inferior performance.

3.2. Comparative Characterization of Carbon Samples

Figure 1a–f presents the morphological characteristics of the obtained carbon samples. Except for the non-activated sample 2L1A-N, all activated carbons exhibit well-developed porous structures, highlighting the crucial role of KOH activation in pore generation. Distinct sheet-like or layered features are observed in 1L1A and 2L1A, whereas the intersheet spaces become partially closed in 3L1A. This evolution is likely associated with the reduced structural rigidity provided by AL and the intensified rearrangement of carbon frameworks during pyrolysis, resulting in a gradual transition from an open layered architecture to a denser carbon matrix [25]. In contrast, L-K exhibits a relatively compact morphology without obvious interconnected features (Figure 1e), indicating that the mixed-lignin precursor is more favorable for constructing an integrated carbon framework. TEM images of 2L1A show abundant pores distributed throughout the carbon matrix (Figure 1g,i,k). Numerous ultrathin carbon nanosheets with lateral dimensions exceeding 100 nm are clearly identified (Figure 1h,i), consistent with the layered morphology seen in the SEM images. These nanosheets divide the pore space into interconnected hierarchical structures (Figure 1i). High-resolution TEM (HRTEM) images predominantly show pseudo-graphitic layers with a few locally graphitized domains (Figure 1j,l). The corresponding Fast Fourier Transform (FFT) pattern (Figure S6) presents hexagonally arranged diffraction spots, indicating relatively high graphitic ordering within the selected region (green dot) [26]. A gradual reduction in structural ordering from the interior toward the outer region can also be observed in Figure 1j, suggesting a higher defect density near exposed surfaces. This structural feature is favorable for improving electrical conductivity and facilitating ion transport [17]. Energy-dispersive X-ray spectroscopy (EDS) elemental mappings (Figure 1m–p) further show that C, O, and S are uniformly distributed throughout the carbon framework.

As illustrated in Figure 2a, all activated carbons exhibit hybrid Type I/IV adsorption–desorption isotherms, confirming that KOH activation generated a hierarchical pore network dominated by micropores while retaining a considerable proportion of mesopores [12]. In addition, the H4 hysteresis loop appearing at $P/P_0 \approx 0.45$–0.90, together with the continuous increase in N_2 uptake at higher relative pressures, suggests that the porous framework also contains larger transport pores extending into the macropore range [27,28]. This is consistent with the SEM results. Such a hierarchical pore network is advantageous for electrochemical charge storage because pores of different sizes fulfill complementary functions. The abundant micropores maximize ion adsorption, while interconnected mesopores and larger transport pores facilitate electrolyte infiltration and accelerate ion diffusion, thereby improving both charge-storage efficiency and rate performance [29,30]. The pore-size distribution curves (Figure 2b) together with the textural parameters summarized in Table 1 further confirm the formation of well-developed hierarchically porous structures in all activated samples, with SSA exceeding 1000 $m^2\ g^{-1}$ and mesopore volumes exceeding micropore volumes. Despite the nearly unchanged SSA with increasing LS content, the total

pore volume exhibits a volcano-like trend and reaches a maximum at an LS/AL ratio of 1:1, suggesting that lignin composition primarily regulates pore-size distribution rather than accessible surface area. Moderate incorporation of LS likely promotes pore enlargement and mesopore development during carbonization, resulting in the highest pore volume for the 1:1 sample. Further increasing the LS proportion facilitates micropore generation while preserving a considerable volume of mesopores, leading to a gradual redistribution of the hierarchical pore structure. Consequently, the micropore fraction increases in the 2:1 and 3:1 samples, accompanied by a slight decrease in total pore volume. Nevertheless, the coexistence of increased microporosity and a substantial mesopore contribution suggests a more balanced pore configuration, which may be more favorable for ion accessibility and transport during capacitive energy-storage processes [31].

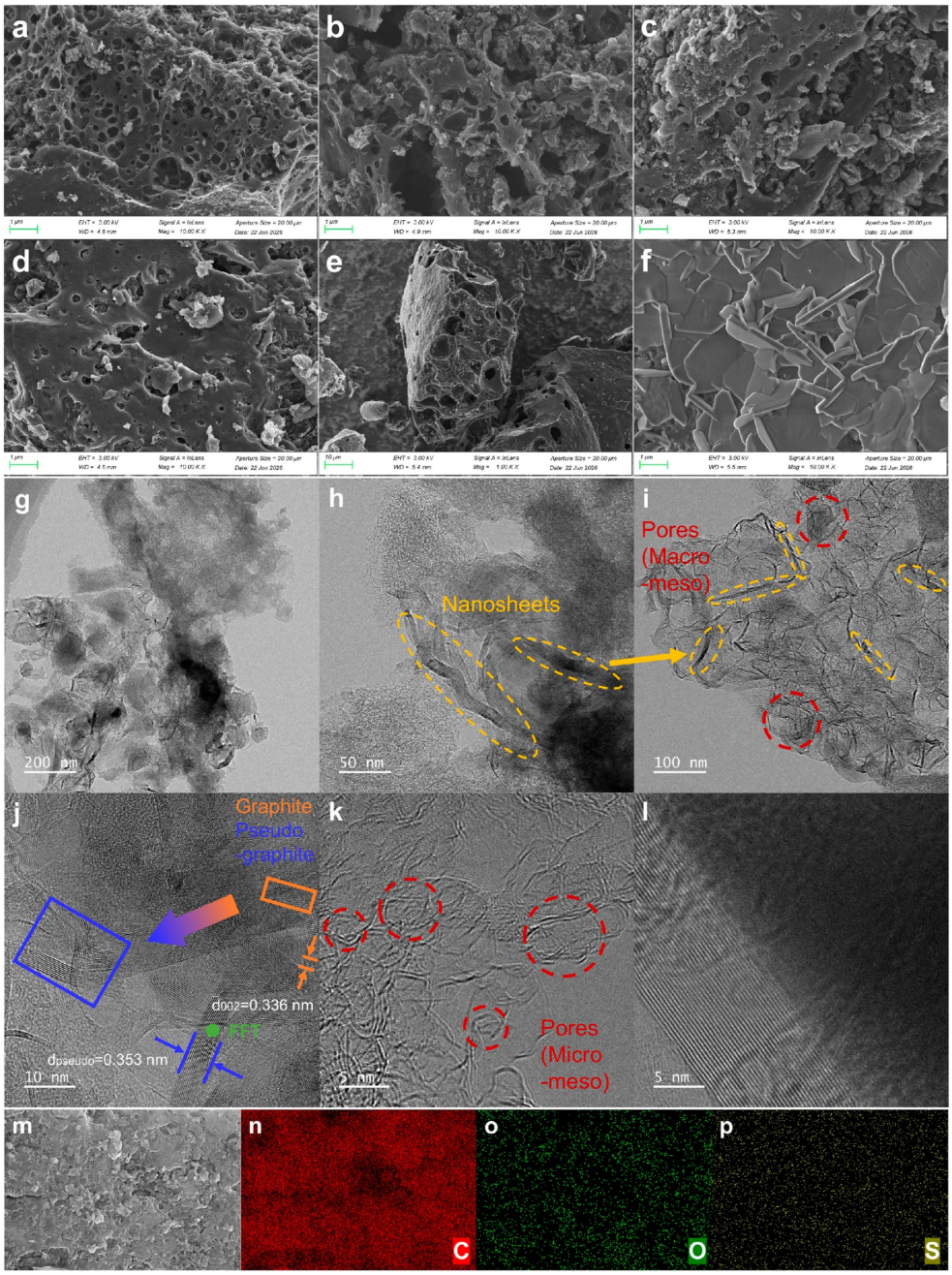


Figure 1. SEM images of (**a**) 1L2A, (**b**) 1L1A, (**c**) 2L1A, (**d**) 3L1A, (**e**) L-K, and (**f**) 2L1A-N; (**g**–**i**) TEM images, (**j**–**l**) HRTEM images, and (**m**–**p**) EDS elemental mappings of the 2L1A.

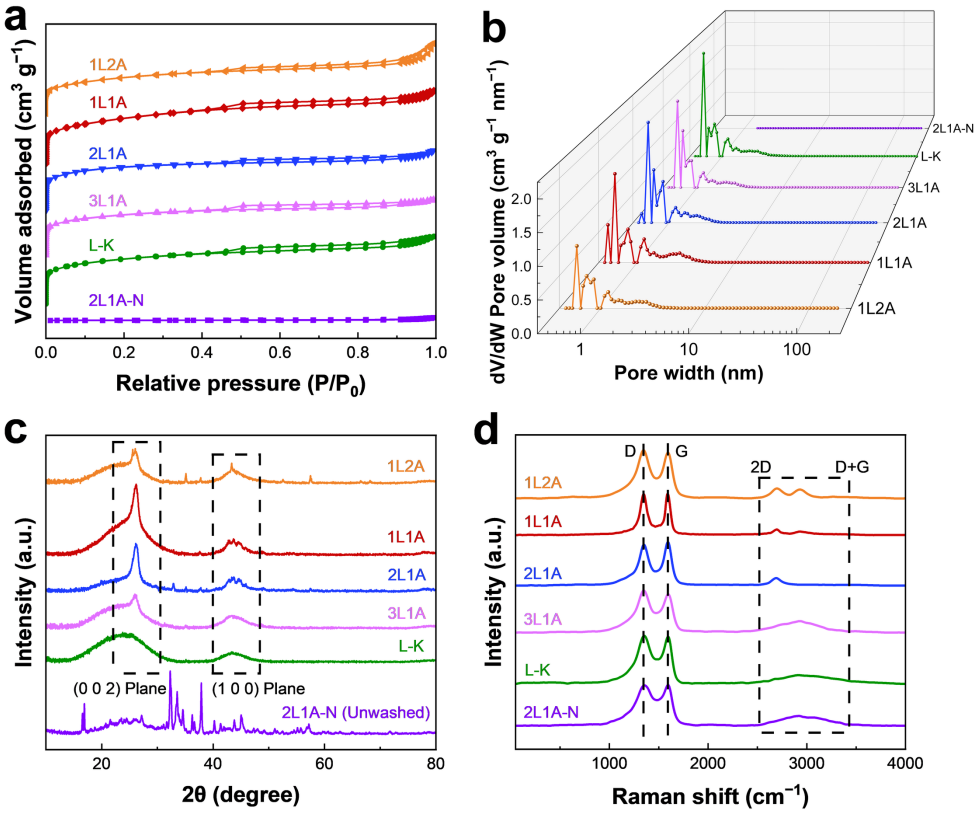


Figure 2. (**a**) N_2 adsorption–desorption isotherms, (**b**) pore-size distributions, (**c**) XRD patterns, and (**d**) Raman spectra of the carbon samples.

Table 1. Textural properties and Raman features of the prepared carbon samples.

Sample	S_{BET} [a] (m^2 g^{-1})	V_{total} [b] (cm^3 g^{-1})	V_{micro} [c] (cm^3 g^{-1})	V_{meso} [d] (cm^3 g^{-1})	V_{meso}/V_{total}	D_{avg} [e] (nm)	I_D/I_G [f]
1L2A	1097.54	0.899	0.089	0.352	0.392	3.28	1.04 ± 0.01
1L1A	1371.27	0.941	0.120	0.420	0.446	2.75	1.01 ± 0.04
2L1A	1363.94	0.779	0.228	0.255	0.327	2.28	0.98 ± 0.02
3L1A	1247.48	0.722	0.201	0.244	0.338	2.31	1.08 ± 0.06
L-K	1378.62	0.868	0.210	0.328	0.378	2.52	1.10 ± 0.03
2L1A-N	7.07	0.036	0.001	0.021	0.583	12.82	1.05 ± 0.01

[a]: Brunauer–Emmett–Teller (BET) surface area. [b]: Total pore volume (V_{total}) was determined using the single-point adsorption method at P/P_0 = 0.9934968. [c]: Micropore volume (V_{micro}) was obtained using the t-plot method. [d]: Mesopore volume (V_{meso}) was calculated by the Barrett–Joyner–Halenda (BJH) method based on the adsorption branch due to a sharp peak at 3.8 nm in the desorption branch. [e]: Average pore diameter was calculated by the 4V/A method, where V and A represent V_{total} and S_{BET}, respectively. [f]: The integral intensity ratio of D-band to G-band after peak fitting (presented as mean ± standard deviation).

Figure 2c presents the XRD patterns of the prepared carbon samples. In contrast to the activated carbons, 2L1A-N is dominated by numerous sharp diffraction peaks, which are attributed to crystalline inorganic species retained after pyrolysis. These inorganic residues are effectively removed following KOH activation and washing, leaving only the (002) and (100) reflections characteristic of partially graphitized carbon in the activated samples. The retained mineral species are expected to function as intrinsic activation promoters or self-templating components during the subsequent KOH activation process, facilitating carbon etching and pore development [32]. Among the activated samples, 2L1A exhibits the most pronounced (002) and (100) reflections, suggesting a relatively higher degree of local structural ordering and turbostratic stacking [33]. This behavior may be associated

with the complementary roles of AL and LS during carbonization. Specifically, the relatively rigid aromatic framework provided by AL favors the development of locally ordered carbon domains, whereas the decomposition of LS promotes structural evolution through volatile release. An appropriate balance between these two effects may facilitate the development of locally ordered sp^2 carbon domains, while excessive AL suppresses structural rearrangement and excessive LS introduces additional structural disorder. The Raman spectra (Figure 2d) and the corresponding I_D/I_G values (Table 1) further corroborate the XRD results. Among all samples, 2L1A exhibits the lowest I_D/I_G average value of 0.98, consistent with a relatively low degree of disorder among the investigated samples. In addition, a well-defined 2D band accompanied by a substantially weakened (D + G) band is observed for both 2L1A and 1L1A, whereas 1L2A exhibits distinguishable 2D and (D + G) bands. By comparison, these two features gradually merge into a broad hump in 3L1A, L-K, and 2L1A-N, indicating reduced stacking order of graphene-like layers [34,35]. These observations are in good agreement with the pseudo-graphitic domains and locally ordered carbon structures identified by HRTEM. Overall, the optimized LS/AL ratio appears to favor microstructural evolution toward locally ordered carbon domains and more pronounced pseudo-graphitic characteristics in 2L1A, which are expected to contribute to efficient charge transport and favorable ion accessibility, thereby benefiting electrochemical energy storage.

The XPS survey spectra of all samples are presented in Figure 3a. Together with Table S2, it can be seen that C and O are the dominant surface elements, whereas S is present in relatively low concentrations. After charge correction, the high-resolution C 1s and O 1s spectra were deconvoluted, as shown in Figure S7 and Figure S8. The C 1s spectra exhibit generally consistent fitting results among all samples. A notable difference is observed for samples with an LS/AL ratio above 2, where the π–π* satellite peak around 290 eV disappears and is replaced by an O–C=O component at approximately 288.5 eV [36]. Since the π–π* satellite originates from the excitation of delocalized π electrons in aromatic sp^2 carbon domains, this transformation suggests a reduced degree of π-electron conjugation and graphitic ordering [37], consistent with the XRD and Raman results. In comparison, the unactivated 2L1A-N exhibits four distinguishable C 1s components, whereas only three components remain after activation, indicating that the high-temperature activation process consumes part of the original surface functional groups. The O 1s spectra were resolved into three components assigned to C=O (~531.5 eV), C–O (~532.5 eV), and O–C=O (~533.5 eV) [38]. These oxygen-containing functional groups not only contribute to pseudocapacitive reactions but also improve the surface wettability of the carbon electrode, thereby facilitating ion transport [39]. Notably, 2L1A possesses the highest O content, suggesting that the synergistic interaction between LS and AL, at an appropriate mixing ratio, favors the retention of the highest amount of oxygen-containing functional groups, thereby providing a surface chemistry more favorable for electrolyte accessibility and charge storage.

The variation in surface S content among different samples is summarized in Figure 3b. Complementary bulk elemental analysis of 2L1A shows a S content of 0.854 wt.%, while the residual Na and K contents are 0.0463 and 0.0974 wt.%, respectively (Table S3). These results provide independent evidence for sulfur retention and indicate that Na and K are effectively removed during the washing process. A pronounced decrease in S content is observed when the LS/AL ratio exceeds 1. Interestingly, the activated L-K sample retains a higher S content than the unactivated 2L1A-N sample, suggesting that S retention is influenced by both the initial S content and the thermal treatment conditions. Figure 3c–h presents the deconvoluted S 2p spectra of the representative samples. For all samples other than 1L1A, the S 2p spectra are reasonably described by two constrained spin–orbit doublets, each consisting of an S $2p_{3/2}$ and an S $2p_{1/2}$ component. The lower-binding-energy

doublet at approximately 163–165 eV is assigned to thiophene-S (C–S–C), while the higher-binding-energy doublet at approximately 168–170 eV is assigned to oxidized-S (–SO_x–) [12]. Thiophene-S has been generally associated with enhanced electronic conductivity and modulation of the electronic structure of carbon materials, while oxidized-S species can increase surface polarity and wettability and may provide additional redox-active sites, thereby potentially contributing to charge storage [40,41]. The relative distributions of S species are summarized in Figure 3i. For 1L2A and 2L1A, thiophene-S is relatively dominant, accounting for 59–61% of the fitted S signal, whereas the proportion of oxidized-S increases substantially in 3L1A, reaching approximately 59%. L-K exhibits the highest proportion of thiophene-S (~80%), while 2L1A-N is dominated by oxidized-S (~63%). These results indicate that the surface S configuration varies with the lignin precursor composition and thermal treatment conditions rather than following a simple monotonic trend. In contrast, the S 2p signal of 1L1A is weak and highly broadened and is therefore presented as an unresolved S 2p signal without assigning specific S species. Overall, the mixed-lignin strategy modifies the relative distribution of surface S species, particularly favoring a higher proportion of oxidized-S compared with the pure-LS-derived L-K sample. This altered S configuration, together with the hierarchical pore structure and oxygen-containing surface functionalities, may contribute to the electrochemical performance of the carbon electrodes. Detailed peak-fitting parameters for the C 1s, O 1s, and S 2p spectra are provided in Tables S4–S9 for reference.

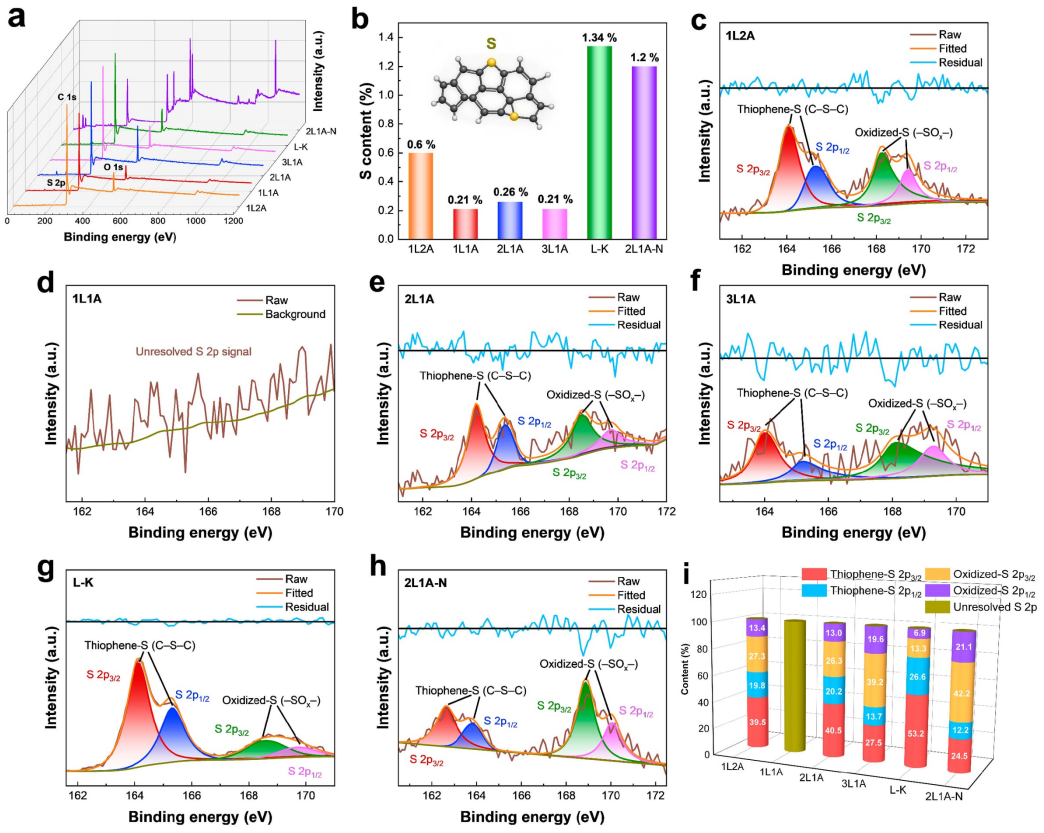


Figure 3. (**a**) XPS survey spectra and (**b**) S content of different carbon samples; high-resolution S 2p spectra of (**c**) 1L2A, (**d**) 1L1A, (**e**) 2L1A, (**f**) 3L1A, (**g**) L-K, and (**h**) 2L1A-N; and (**i**) relative distribution of different S species in the carbon samples.

3.3. Electrochemical Performance Evaluation

The excellent physicochemical characteristics of the mixed-lignin-derived carbons suggest their considerable potential as electrode materials for supercapacitors. Their elec-

trochemical performance was initially evaluated in a conventional three-electrode system with 6 M KOH serving as the electrolyte. As illustrated in Figure 4a, all samples exhibit nearly rectangular cyclic voltammetry (CV) curves at a scan rate of 50 mV s^{-1}, indicative of typical electric double-layer capacitive (EDLC) behavior [42]. Among them, 2L1A encloses the largest enclosed CV area and a CV-derived gravimetric capacitance (C_v) of 389.7 F g^{-1} (Equation (S1)) [12]. Furthermore, the CV curves of 2L1A remain highly symmetric over a wide range of scan rates with only a gradual transition from a quasi-rectangular to a diamond-like profile and no obvious distortion (Figure 4b). Such behavior suggests highly reversible charge storage and efficient ion transport within the hierarchically porous carbon framework [12]. Figure 4c presents the galvanostatic charge–discharge (GCD) responses of each sample recorded at 1 A g^{-1}. All electrodes display nearly symmetric triangular profiles, consistent with the highly reversible capacitive behavior revealed by the CV measurements. Among them, 2L1A again delivers the highest GCD gravimetric capacitance (C_g) of 386.7 F g^{-1} ((Equation (S2)) [12]. Although the discharge duration of 2L1A is only slightly longer than that of 3L1A, its substantially larger CV response suggests more favorable charge-storage kinetics [43], which will be further discussed in the following section. Moreover, neither the CV nor the GCD curves exhibit ideal rectangular or perfectly triangular shapes, respectively. These deviations may reflect EDLC behavior accompanied by possible minor pseudocapacitive contributions from oxygen- and sulfur-containing as well as other potentially active surface functional groups. The rate capability of different electrodes was further evaluated based on the GCD results (Figure 4d,e). Although 3L1A exhibits a slightly higher C_g than 2L1A at 0.5 A g^{-1} (458.2 versus 441.9 F g^{-1}), its capacitance decreases much more rapidly with increasing current density. In contrast, 2L1A maintains a capacitance retention exceeding 70% at 20 A g^{-1}, whereas that of 3L1A decreases to only 62%, with the remaining samples showing even poorer rate performance. Consequently, 2L1A exhibits the highest C_g over almost the entire current-density range, demonstrating its superior rate capability. This outstanding performance is reasonably attributed to its well-balanced hierarchical pore structure together with its relatively higher structural ordering, both of which facilitate efficient ion diffusion and electron transport. Compared with lignin-derived carbon electrodes reported over the past two years, 2L1A exhibits a distinctly higher C_g in the three-electrode configuration, highlighting its outstanding charge-storage capability (Table S10) [7,10,11,14,44–61]. To further evaluate the internal resistance of the electrodes, the equivalent series resistance (ESR) was calculated from the IR_{drop} of the GCD curves at different current densities (Figure 4f) [17]. The slope of the IR_{drop} versus current density corresponds to (mR) (Ω g), and the ESR was calculated by dividing this slope by the corresponding active-material mass (m). The calculated ESR values are presented in Table S11. The unactivated 2L1A-N exhibits the highest ESR, whereas the activated samples show lower ESR values ranging from 1.04 to 1.55 Ω, indicating improved electrical transport after KOH activation. To further probe the charge-transfer characteristics of the optimized electrode, electrochemical impedance spectroscopy (EIS) was performed on 2L1A, and the corresponding Nyquist plot and equivalent circuit are shown in Figure S9. The fitted results reveal a low solution resistance (R_s) of 0.61 Ω and an exceptionally small charge-transfer resistance (R_{ct}) of only 0.017 Ω, indicating highly efficient interfacial electron/ion transport with negligible charge-transfer limitation.

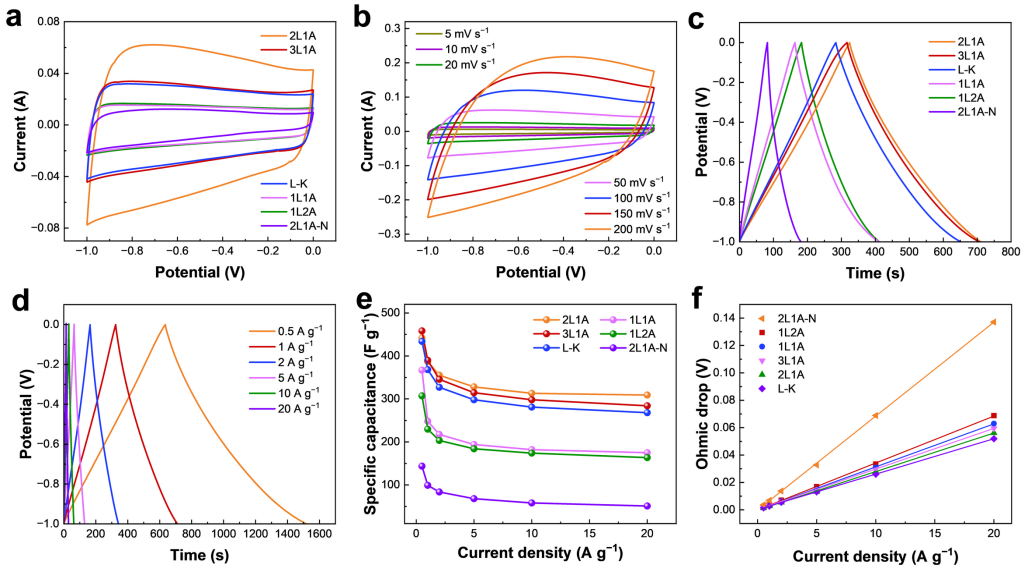


Figure 4. Electrochemical performance of different samples in the three-electrode system. (**a**) CV curves at 50 mV s^{-1} and (**b**) CV curves of 2L1A at various scan rates. (**c**) GCD curves at 1 A g^{-1} and (**d**) GCD curves of 2L1A at various current densities. (**e**) $\mathbf{C_g}$ as a function of current density and (**f**) IR_{drop} curves at different current densities.

To gain further insight into the origin of the superior electrochemical performance of 2L1A, its charge-storage kinetics were systematically investigated. The mixed capacitive behavior was first evaluated by examining how the current response (i) varies with scan rate (v) using Equations (S5) and (S6) [6], from which the b values at different potentials were determined (Figure 5a,b). The b values on the anodic branch are generally higher than those on the cathodic branch and increase at potentials away from the potential reversal points of the CV curves. Generally, a surface-controlled capacitive process is characterized by a b value close to 1, whereas diffusion-controlled charge storage is associated with a b value approaching 0.5 [12]. Notably, the b values of 2L1A remain close to 1 over the entire potential range, indicating that the charge-storage process is governed by mixed capacitive behavior with a predominant surface-controlled contribution. Based on the above results, the Dunn method was further employed to quantitatively distinguish the surface-controlled and diffusion-controlled capacitance contributions using Equations (S7) and (S8) [62]. As shown in Figure 5c, the surface-controlled contribution continuously increases with increasing scan rate and exceeds 90% at 100 mV s^{-1}, demonstrating that rapid charge storage is predominantly sustained by readily accessible surface-controlled processes even under high-rate conditions. Figure 5d presents a representative deconvolution of the capacitive contribution at 50 mV s^{-1}, where the shaded region corresponds to the surface-controlled contribution. The contribution ratios at all scan rates were calculated using the same procedure. Furthermore, the surface-controlled capacitance contributions of electrodes prepared with different LS/AL ratios were compared (Figure S10). All mixed-lignin-derived carbon electrodes exhibit predominantly surface-controlled charge storage, suggesting that the mixed-lignin strategy effectively generates abundant electrochemically accessible charge-storage sites. With increasing LS/AL ratio, the surface-controlled contribution first increases and reaches a maximum for 2L1A, consistent with its optimized pore structure and relatively higher structural ordering. Finally, the charge accessibility of 2L1A was further evaluated using the Trasatti method (Equations (S9)–(S11)) [63], and the fitting results are presented in Figure S11. The outer-surface charge contribution reaches 73.6%, indicating that a substantial fraction of the total accessible charge is associated with the outer surface. This result is consistent with the surface-controlled contribution identified by

the above. Nevertheless, it should be noted that neither the Dunn nor the Trasatti analysis directly distinguishes EDLC from pseudocapacitance.

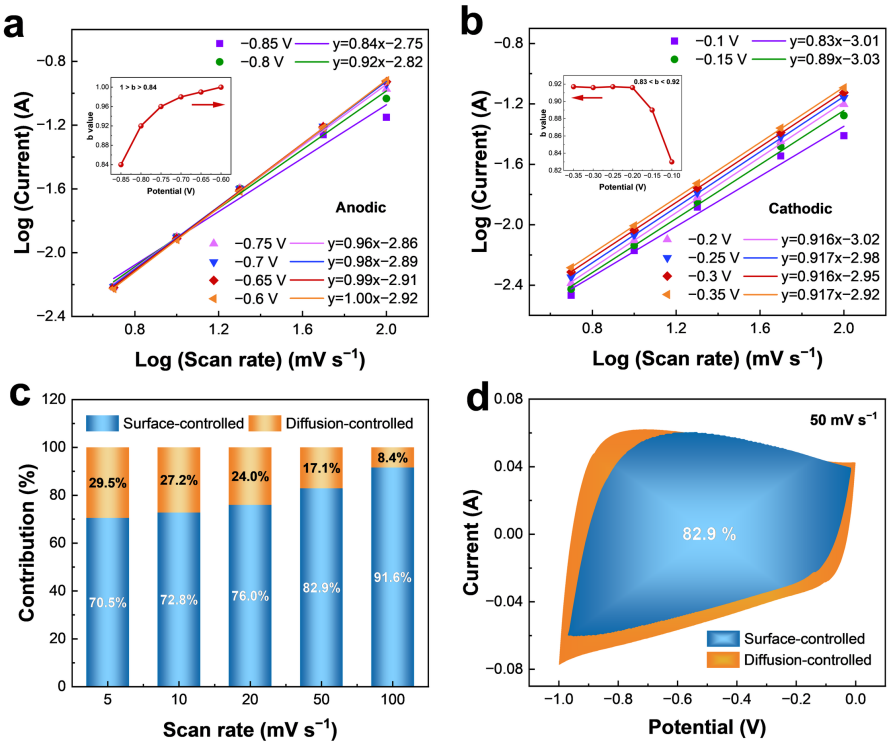


Figure 5. Kinetic analysis of the optimized 2L1A electrode. Current–scan rate logarithmic (log(i)–log(v)) plots at different potentials for the (**a**) anodic and (**b**) cathodic scans (insets: corresponding b-value profiles as a function of potential). (**c**) Stacked contributions of surface-controlled and diffusion-controlled capacitance across various scan rates. (**d**) Surface-controlled capacitive contribution at 50 mV s^{-1} highlighted by the blue shaded area.

A CR2032 coin-type SSC was assembled using two identical 2L1A electrodes to evaluate its practical electrochemical performance. As shown in Figure 6a, the CV curves maintain a nearly rectangular shape with only negligible polarization up to 1.3 V. When the cell voltage is further extended, the polarization gradually becomes more pronounced and increases markedly as the voltage approaches 1.5 V, indicating the increasing contribution of parasitic reactions associated with the practical voltage limit of the KOH aqueous electrolyte. Therefore, 1.3 V was selected as the operating voltage window for subsequent measurements in 6 M KOH. The corresponding CV curves at different scan rates and GCD curves at various current densities are presented in Figure 6b,c, respectively, both exhibiting highly symmetric profiles. To further extend the operating voltage window, the electrolyte was replaced with 1 M Na_2SO_4. As shown in Figure 6d, the maximum cell voltage was successfully expanded to 1.7 V, within which only negligible polarization was observed, demonstrating the excellent voltage tolerance of the 2L1A//2L1A SSC. The corresponding CV and GCD profiles obtained over a range of scan rates and current densities are displayed in Figure 6e,f, respectively. It is worth noting that the Na_2SO_4 electrolyte produces more symmetric CV and GCD profiles than the KOH electrolyte, indicating higher electrochemical reversibility under the wider operating voltage window [6]. This behavior is also reflected by the nearly identical charge and discharge durations, corresponding to an improved Coulombic efficiency. The charge-storage mechanism of the assembled SSC was further examined using the Trasatti method, and the corresponding fitting results are presented in Figure S12. In the KOH electrolyte, the outer-surface charge contribution is 73.1% of the total accessible capacitance, which is in excellent agree-

ment with the three-electrode kinetic analysis. When the electrolyte is replaced with 1 M Na_2SO_4, the outer-surface charge contribution decreases to 63.6%, while still remaining the dominant charge-storage mechanism. The reduced outer-surface charge contribution may be associated with the expanded operating voltage window, which may allow a greater contribution from other charge-storage processes potentially involving the oxygen- and sulfur-containing and other surface functional groups [39]. Consequently, these possible contributions may lower the relative outer-surface charge contribution without altering the dominant role of outer-surface charge storage in the overall capacitance.

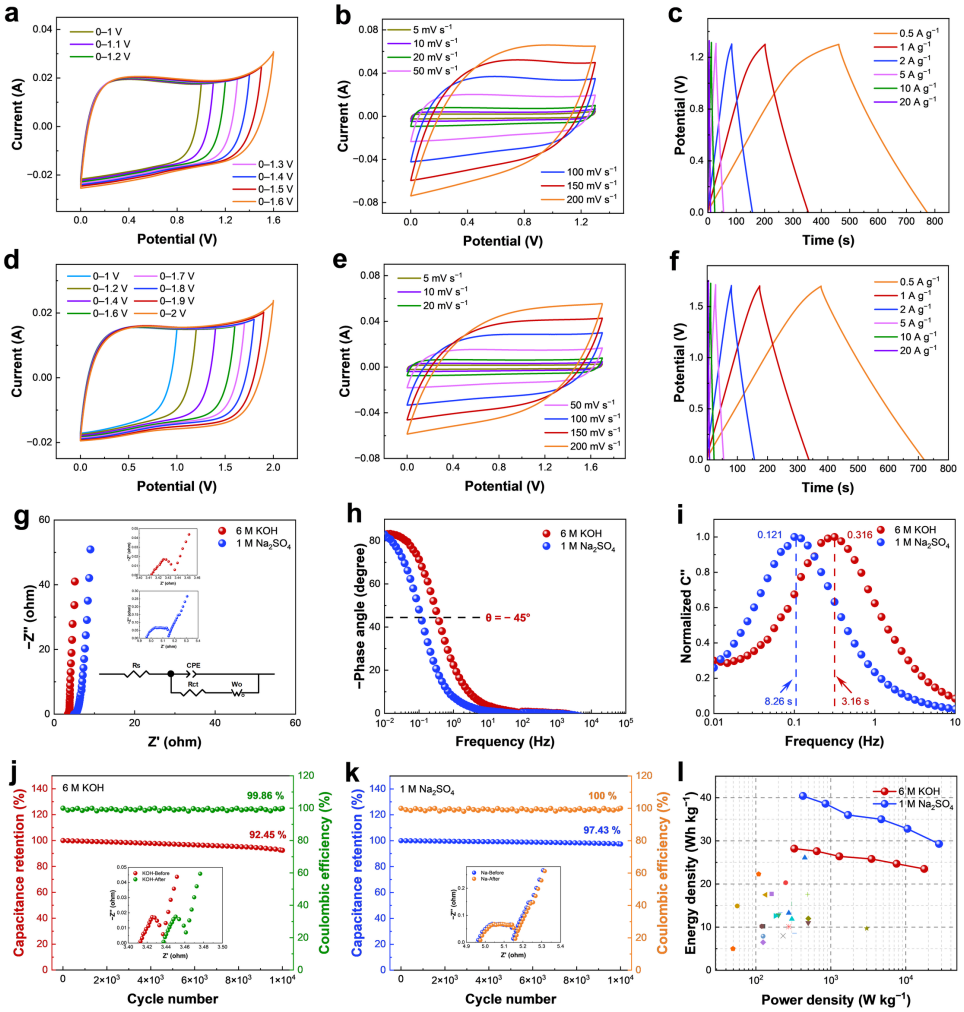


Figure 6. Electrochemical performance of the 2L1A//2L1A SSC. (**a**) CV curves recorded under different operating voltage windows in 6 M KOH. (**b**) CV curves at different scan rates and (**c**) GCD curves at various current densities within the selected operating voltage window in 6 M KOH. (**d**) CV curves recorded under different operating voltage windows in 1 M Na_2SO_4. (**e**) CV curves at different scan rates and (**f**) GCD curves at various current densities within the selected operating voltage window in 1 M Na_2SO_4. (**g**) Nyquist plots of the SSC in different electrolytes (inset: enlarged high-frequency region and equivalent circuit). (**h**) Bode phase plots and (**i**) normalized imaginary capacitance (C″) as a function of frequency. Cycling stability over 10,000 charge–discharge cycles at 5 A g^{-1} in (**j**) 6 M KOH and (**k**) 1 M Na_2SO_4 (insets: Nyquist plots before and after cycling). (**l**) Ragone plot in comparison with recently reported lignin-derived symmetric supercapacitors.

The electrochemical impedance spectroscopy (EIS) results of the 2L1A//2L1A SSC in different electrolytes are presented in Figure 6g. According to the fitted results, the KOH electrolyte exhibits lower R_s (3.42 Ω versus 4.97 Ω) and R_{ct} (0.021 Ω versus 0.20 Ω) than the Na_2SO_4 electrolyte. This behavior can be attributed to the higher ionic conductivity of KOH

together with the faster transport of hydrated K^+ ions within the hierarchically porous carbon framework [64]. Consistent with the three-electrode measurements, the R_{ct} values remain much smaller than the corresponding R_s values, indicating that interfacial R_{ct} is negligible and the overall impedance is predominantly governed by the R_s. Moreover, the nearly vertical low-frequency region of the Nyquist plots and the phase angles approaching 90 ° in the Bode plots (Figure 6h) further demonstrate excellent capacitive behavior, efficient ion diffusion, and highly reversible charge storage [17]. The imaginary capacitance (C'') was further calculated according to Equations (S12)–(S15). Based on the peak frequencies of the C'' curves, the corresponding relaxation times (τ) were determined to be 3.16 s and 8.26 s for the KOH and Na_2SO_4 electrolytes, respectively (Figure 6i and Equation (S16)) [65]. The shorter relaxation time indicates a faster transition from resistive to capacitive behavior and more rapid charge/discharge kinetics. Therefore, the SSC exhibits a faster electrochemical response in the KOH electrolyte, consistent with its lower impedance and superior rate capability.

The long-term cycling stability of the assembled 2L1A//2L1A SSC was evaluated over 10,000 charge–discharge cycles at 5 A g^{-1} in both electrolytes, and the corresponding capacitance retention and Coulombic efficiency are presented in Figure 6j,k. The Coulombic efficiency, defined as the ratio of discharge to charge quantities, reflects charge–discharge reversibility and is distinct from energy efficiency, which accounts for energy losses during charge–discharge cycling. After prolonged cycling, the SSC retains 92.45% of its initial capacitance in 6 M KOH, while a higher retention of 97.43% is achieved in 1 M Na_2SO_4. Meanwhile, the Coulombic efficiencies remain nearly constant at 99.86% and approximately 100%, respectively, demonstrating the excellent reversibility and durability of both devices. The superior cycling stability in the Na_2SO_4 electrolyte is likely associated with its milder electrochemical environment, which effectively suppresses irreversible side reactions and structural degradation during repeated charge–discharge processes [66]. This result is also consistent with the more symmetric GCD profiles observed previously, further confirming the highly reversible charge-storage behavior of the SSC in the neutral electrolyte. The Coulombic efficiency remaining close to 100% throughout cycling indicates highly reversible charge–discharge behavior, suggesting limited irreversible charge loss during repeated cycling [67]. To further assess the suitability of the selected voltage windows, leakage-current measurements were performed at 1.3 V in 6 M KOH and 1.7 V in 1 M Na_2SO_4, as shown in Figure S13. In both electrolytes, the leakage current rapidly decreased from its initial value and then stabilized at a relatively low sub-milliampere level, reaching approximately 0.836 mA in KOH and 0.357 mA in Na_2SO_4. These results indicate relatively low and stable leakage currents under the tested conditions, providing supplementary evidence in support of the selected voltage windows. The Nyquist plots before and after cycling, shown in the insets of Figure 6j,k, exhibit nearly identical profiles with only a slight shift toward higher resistance after prolonged cycling, while the change in the Na_2SO_4 electrolyte is even less pronounced. This minor increase in impedance is reasonably attributed to slight interfacial aging together with a small increase in contact and electrolyte resistance during long-term operation, whereas the overall charge-transport characteristics remain essentially unchanged [68,69]. These results further verify the outstanding structural robustness and electrochemical stability of the assembled SSC, particularly in the Na_2SO_4 electrolyte. Based on the C_g obtained from the GCD measurements (Figure 6c,f), the corresponding energy and power densities were calculated according to Equations (S3) and (S4). In the 1 M Na_2SO_4 electrolyte, the assembled SSC delivers a high energy density of 40.4 Wh kg^{-1} at a power density of 424.8 W kg^{-1} and retains 29.3 Wh kg^{-1} even at a high power density of 27,757.9 W kg^{-1}, demonstrating its excellent capability for simultaneously achieving high energy and high power output.

Even in the 6 M KOH electrolyte with a narrower operating voltage window, the device still achieves an energy density of 28.2 Wh kg^{-1} at 325.4 W kg^{-1}, which is comparable to or exceeds that reported for some lignin-derived SSCs employing Na_2SO_4 electrolytes. As summarized in Table S12 and illustrated by the Ragone plot in Figure 6l, the assembled SSC exhibits clear advantages over lignin-derived SSCs reported over the past two years [7,10,11,14,45–51,54,56–59,61,70–73], highlighting the effectiveness of the mixed-lignin strategy for constructing high-performance supercapacitors.

Based on the above analyses, the superior electrochemical behavior of 2L1A may be associated with the synergistic structural advantages generated by the mixed-lignin strategy, as schematically illustrated in Figure 7. The appropriate combination of LS and AL promotes homogeneous carbonization and activation, resulting in an interconnected lamellar carbon framework with abundant hierarchical porosity. The ultrathin carbon nanosheets provide sufficient electrochemically accessible surfaces, while the interconnected architecture ensures continuous electron-transport pathways throughout the electrode. Meanwhile, the well-developed hierarchical pore network, featuring interconnected micro-, meso-, and macropores, offers abundant charge-storage sites while simultaneously facilitating electrolyte penetration and shortening ion-diffusion pathways, thereby enabling rapid charge propagation even at high current densities. In addition, the relatively higher structural ordering together with the partially graphitized carbon domains is expected to enhance the electrical conductivity of the carbon framework without sacrificing the defect sites required for efficient ion adsorption. The coexistence of oxygen- and sulfur-containing functional groups potentially improves electrode wettability and may contribute to additional pseudocapacitive charge storage, hypothetically favoring a synergistic combination between EDLC and pseudocapacitance. More importantly, the robust interconnected carbon framework could effectively buffer structural stress during repeated charge–discharge processes, thereby presumably maintaining the integrity of the porous architecture and ensuring excellent cycling durability. The synergistic integration of these structural and compositional characteristics is envisioned to endow 2L1A with fast electron transport, efficient electrolyte-ion diffusion, abundant electrochemically active sites, and highly reversible charge-storage behavior, ultimately offering a plausible explanation for its outstanding electrochemical performance.

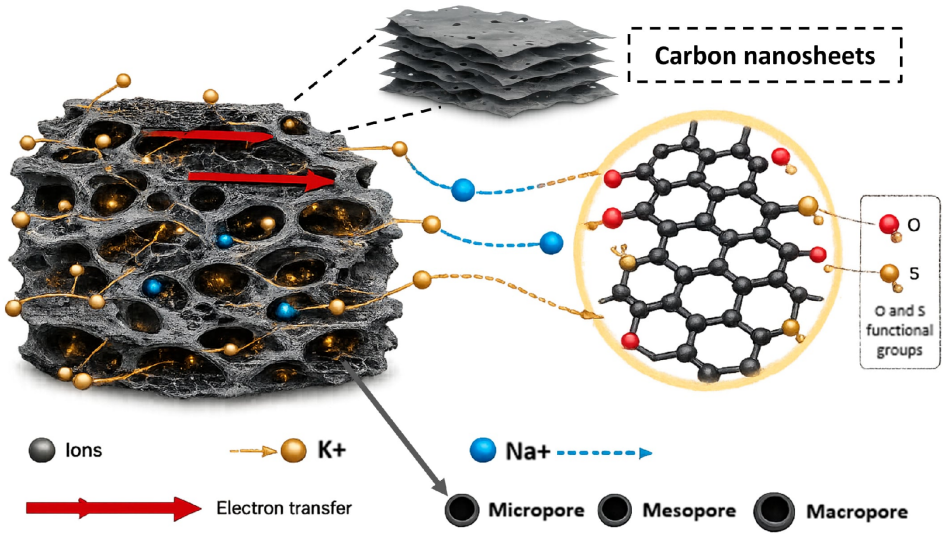


Figure 7. Proposed schematic illustration for the superior electrochemical performance of the 2L1A electrode.

4. Conclusions

A mixed dual-lignin precursor strategy was demonstrated as an effective route for producing high-performance biomass-derived carbon electrodes through ex situ carbonization followed by KOH activation, whereas the in situ activation route failed to generate the desired porous carbon. Among the investigated precursor compositions, the LS/AL mass ratio of 2 provided the most favorable balance between carbon yield and structural evolution, producing interconnected carbon nanosheets with an SSA of 1363.9 m^2 g^{-1}, a well-developed hierarchical pore network, and an appropriate degree of graphitic ordering dominated by pseudo-graphitic domains. XPS analyses further revealed that the mixed-lignin strategy altered the relative distribution of surface S species while promoting the retention of abundant oxygen-containing functionalities in 2L1A, providing favorable surface chemistry that may contribute to the electrochemical performance of the carbon electrodes. As a result, the optimized 2L1A electrode achieved a C_g of 386.7 F g^{-1} at 1 A g^{-1}. The corresponding SSCs yielded high energy densities of 28.2 Wh kg^{-1} in 6 M KOH and 40.4 Wh kg^{-1} in 1 M Na_2SO_4, together with outstanding cycling durability. Electrochemical and kinetic analyses indicate that the superior capacitive behavior is attributed to the synergistic optimization of hierarchical pore architecture, graphitic ordering, and surface chemistry, thereby promoting electrolyte accessibility, rapid electron transport, efficient ion diffusion, and predominantly surface-controlled charge storage. These findings provide a clearer understanding of the structure–composition–performance relationship in mixed-lignin-derived carbons and demonstrate that material precursor modulation is an effective strategy for developing high-performance biomass-derived carbon electrodes for supercapacitors.

Supplementary Materials: The following supporting information can be downloaded at: https://www.mdpi.com/article/10.3390/en19204894/s1, Figure S1. (a) CV curve recorded at 50 mV s^{-1} and (b) GCD curves of LAK; (c) CV curve recorded at 50 mV s^{-1} and (d) GCD curves of 2LAK. Figure S2. (a) XRD patterns and (b) Raman spectra of LSPC and ALPC. Figure S3. Homogeneous viscous gel formed after mixing LS and AL. Figure S4. FTIR spectra of LS, AL, and 2LS + 1AL. Figure S5. (a) TG and (b) DTG profiles versus temperature; (c) TG and (d) DTG profiles versus time for LS, AL, 2LS + 1AL, and theoretical 2LS + 1AL. Figure S6. Fast Fourier transform (FFT) pattern of the HRTEM image of 2L1A. Figure S7. High-resolution C 1s XPS spectra of (a) 1L2A, (b) 1L1A, (c) 2L1A, (d) 3L1A, (e) L-K and (f) 2L1A-N. Figure S8. High-resolution O 1s XPS spectra of (a) 1L2A, (b) 1L1A, (c) 2L1A, (d) 3L1A, (e) L-K and (f) 2L1A-N. Figure S9. Nyquist plot of 2L1A in the three-electrode configuration and the corresponding equivalent circuit. Inset: enlarged view of the high-frequency region. Figure S10. Surface-controlled and diffusion-controlled charge-storage contributions of the mixed-lignin-derived samples at 50 mV s^{-1}. Figure S11. Trasatti plots of the three-electrode system: (a) C^{-1} versus $v^{0.5}$ and (b) C versus $v^{-0.5}$. Figure S12. Trasatti plots of the symmetric supercapacitor in (a, b) 6 M KOH and (c, d) 1 M Na_2SO_4 electrolytes: (a, c) C^{-1} versus $v^{0.5}$ and (b, d) C versus $v^{-0.5}$. Figure S13. Leakage current curves of 2L1A//2L1A supercapacitor in 6 M KOH (1.3 V) and 1 M Na_2SO_4 (1.7 V) electrolytes. Table S1. Detailed yield information for different carbon samples. Table S2. Relative element contents of all samples from XPS results. Table S3. Bulk C, H, N, and S contents and residual Na and K contents of 2L1A. Table S4. Deconvolution results of XPS spectra of 1L2A. Table S5. Deconvolution results of XPS spectra of 1L1A. Table S6. Deconvolution results of XPS spectra of 2L1A. Table S7. Deconvolution results of XPS spectra of 3L1A. Table S8. Deconvolution results of XPS spectra of L-K. Table S9. Deconvolution results of XPS spectra of 2L1A-N. Table S10. Comparison of the specific capacitance of 2L1A with recently reported lignin-derived carbon electrode materials based on KOH electrolyte. Table S11. ESR values of samples derived from GCD curves. Table S12. Comparison of the device performance of the 2L1A//2L1A symmetric supercapacitor with recently reported lignin-derived carbon-based supercapacitors.

Author Contributions: C.S.: Conceptualization, Methodology, Investigation, Data curation, Formal analysis, Writing—original draft. Z.L.: Funding acquisition, Supervision, Validation, Writing—review and editing, Resources. S.W.: Conceptualization. Validation, Writing—Review and Editing, Supervision, Resources. C.Y.: Methodology, Investigation, Writing—review and editing, Supervision, Resources. All authors have read and agreed to the published version of the manuscript.

Funding: We gratefully acknowledge financial support from the National Natural Science Foundation of China, No. 52236011.

Data Availability Statement: The original contributions presented in this study are included in the article/Supplementary Materials. Further inquiries can be directed to the corresponding author.

Conflicts of Interest: The authors declare no conflicts of interest.

References

1. Qiu, S.; Chen, Z.; Zhuo, H.; Hu, Y.; Liu, Q.; Peng, X.; Zhong, L. Using FeCl3 as a Solvent, Template, and Activator To Prepare B, N Co-Doping Porous Carbon with Excellent Supercapacitance. *ACS Sustain. Chem. Eng.* **2019**, *7*, 15983–15994. [CrossRef]
2. Ji, D.; Jin, K.; You, Z.; Wei, Y.; Ji, J. Nitrogen-Doped Bamboo-Based Porous Activated Carbon for High-Performance Supercapacitor Electrodes. *Energies* **2026**, *19*, 1199. [CrossRef]
3. Luo, L.; Lan, Y.; Zhang, Q.; Deng, J.; Luo, L.; Zeng, Q.; Gao, H.; Zhao, W. A review on biomass-derived activated carbon as electrode materials for energy storage supercapacitors. *J. Energy Storage* **2022**, *55*, 105839. [CrossRef]
4. Nidheesh, P.V.; Gopinath, A.; Ranjith, N.; Praveen Akre, A.; Sreedharan, V.; Suresh Kumar, M. Potential role of biochar in advanced oxidation processes: A sustainable approach. *Chem. Eng. J.* **2021**, *405*, 126582. [CrossRef]
5. Kwarciany, R.; Fiedur, M.; Saletnik, B. Opportunities and Threats for Supercapacitor Technology Based on Biochar—A Review. *Energies* **2024**, *17*, 4617. [CrossRef]
6. Li, W.; Li, C.; Xu, Y.; Wang, G.; Xu, T.; Zhang, W.; Si, C. Heteroatom-doped and graphitization-enhanced lignin-derived hierarchically porous carbon via facile assembly of lignin-Fe coordination for high-voltage symmetric supercapacitors. *J. Colloid Interface Sci.* **2024**, *659*, 374–384. [CrossRef] [PubMed]
7. Pan, C.; Ji, Y.; Ren, S.; Lei, T.; Dong, L. Lignin-Derived Activated Carbon as Electrode Material for High-Performance Supercapacitor. *Molecules* **2024**, *30*, 89. [CrossRef] [PubMed]
8. Fu, F.; Yang, D.; Zhang, W.; Wang, H.; Qiu, X. Green self-assembly synthesis of porous lignin-derived carbon quasi-nanosheets for high-performance supercapacitors. *Chem. Eng. J.* **2020**, *392*, 123721. [CrossRef]
9. Li, P.; Zhong, W.; Chen, D.; Li, T.; Qian, W.; Wu, W.; Jiang, B. Pyrolysis mechanism unlocks the superior energy storage of amine-functionalized lignin carbon for tailoring porous electrodes. *J. Energy Storage* **2026**, *152*, 120605. [CrossRef]
10. Dong, L.; Zhang, Q.; Ji, Y.; Pan, C.; Xu, F.; Ren, S.; Lei, T. Sol-Gel Coupled KOH Activation Synthesis of Lignin-Derived Hierarchical Porous Carbon: Optimization and Supercapacitor Applications. *ChemistrySelect* **2025**, *10*, e03318. [CrossRef]
11. Liang, Y.; Yu, Y.; Qi, X. Synthesis of hollow hierarchical porous carbon spheres from lignin by soft template and hydrothermal method for supercapacitors. *Int. J. Biol. Macromol.* **2025**, *307*, 141938. [CrossRef] [PubMed]
12. Sun, Y.; Xu, D.; Wang, S. Self-assembly of biomass derivatives into multiple heteroatom-doped 3D-interconnected porous carbon for advanced supercapacitors. *Carbon* **2022**, *199*, 258–267. [CrossRef]
13. Yuan, M.; Zhang, Y.; Niu, B.; Jiang, F.; Yang, X.; Li, M. Chitosan-derived hybrid porous carbon with the novel tangerine pith-like surface as supercapacitor electrode. *J. Mater. Sci.* **2019**, *54*, 14456–14468. [CrossRef]
14. Wang, C.; Qiao, J.; Chen, B.; Ge, Y.; Li, Z.; Qiu, X. In-Situ Gas Exfoliation Chemistry Engineering of Oxygen/Nitrogen-Functionalized Porous Carbon Nanosheet Frameworks for Supercapacitors. *ACS Appl. Mater. Interfaces* **2026**, *18*, 10003–10015. [CrossRef] [PubMed]
15. Tang, Q.; Zhou, M.; Yang, D.; Qiu, X. Effects of pH on aggregation behavior of sodium lignosulfonate (NaLS) in concentrated solutions. *J. Polym. Res.* **2015**, *22*, 50. [CrossRef]
16. Migunova, A.; Gabdullin, M.; Nemkayeva, R.; Abdullin, K. High-Performance Asymmetric Supercapacitor Based on a Bilayer Cu0.7Zn0.3CoNiSyO4−y/Ni3S2 Electrode. *Energies* **2025**, *18*, 4348. [CrossRef]
17. Sun, Y.; He, Z.; Fan, H.; Wang, S. Nitrogen configuration modulation of porous graphitic carbon nanosheets for superior capacitive energy storage. *J. Power Sources* **2024**, *614*, 235027. [CrossRef]
18. Han, X.; Wei, Q.; Su, Y.; Che, G.; Zhou, J.; Li, Y. Molecular Modification of Lignin-Based Carbon Materials: Influence of Supramolecular Bonds on the Properties. *ACS Appl. Mater. Interfaces* **2023**, *15*, 1969–1983. [CrossRef] [PubMed]
19. Li, P.; Zhou, Z.; Zheng, G.; Shao, Z.; Zhang, Y.; Xu, Y.; Jiang, M.; Zhang, X. Fully Biobased Lignin-Bonded Bamboo Composites with Mold Resistance Based on Lignin Recycle Strategy. *ACS Sustain. Chem. Eng.* **2025**, *13*, 15935–15946. [CrossRef]

20. Huang, Y.; Wang, L.; Chao, Y.; Nawawi, D.S.; Akiyama, T.; Yokoyama, T.; Matsumoto, Y. Analysis of Lignin Aromatic Structure in Wood Based on the IR Spectrum. *J. Wood Chem. Technol.* **2012**, *32*, 294–303. [CrossRef]
21. Tosin, K.G.; Finimundi, N.; Poletto, M. A Systematic Study of the Structural Properties of Technical Lignins. *Polymers* **2025**, *17*, 214. [CrossRef] [PubMed]
22. Kalami, S.; Arefmanesh, M.; Master, E.; Nejad, M. Replacing 100% of phenol in phenolic adhesive formulations with lignin. *J. Appl. Polym. Sci.* **2017**, *134*, 45124. [CrossRef]
23. Zhao, Z.; Cannon, F.S.; Nieto-Delgado, C. Synergistic interaction between lignin and collagen during co-pyrolysis. *Carbon* **2019**, *154*, 254–265. [CrossRef]
24. Boroujeni, F.M.; Fioravanti, G.; Kander, R. Synthesis and Characterization of Cellulose Microfibril-Reinforced Polyvinyl Alcohol Biodegradable Composites. *Materials* **2024**, *17*, 526. [CrossRef] [PubMed]
25. Wang, H.; Feng, P.; Fu, F.; Yu, X.; Yang, D.; Zhang, W.; Niu, L.; Qiu, X. Lignin-derived carbon materials for catalysis and electrochemical energy storage. *Carbon Neutraliz.* **2022**, *1*, 277–297. [CrossRef]
26. Li, J.; Qin, Y.; Shen, J.; Chen, Y. Evolution of carbon nanostructures during coal graphitization: Insights from X-ray diffraction and high-resolution transmission electron microscopy. *Energy* **2024**, *290*, 130316. [CrossRef]
27. Wang, J.G.; Liu, H.; Zhang, X.; Li, X.; Liu, X.; Kang, F. Green Synthesis of Hierarchically Porous Carbon Nanotubes as Advanced Materials for High-Efficient Energy Storage. *Small* **2018**, *14*, e1703950. [CrossRef] [PubMed]
28. Ran, F.; Yang, X.; Xu, X.; Li, S.; Liu, Y.; Shao, L. Green activation of sustainable resources to synthesize nitrogen-doped oxygen-riched porous carbon nanosheets towards high-performance supercapacitor. *Chem. Eng. J.* **2021**, *412*, 128673. [CrossRef]
29. Hao, P.; Zhao, Z.; Leng, Y.; Tian, J.; Sang, Y.; Boughton, R.I.; Wong, C.P.; Liu, H.; Yang, B. Graphene-based nitrogen self-doped hierarchical porous carbon aerogels derived from chitosan for high performance supercapacitors. *Nano Energy* **2015**, *15*, 9–23. [CrossRef]
30. Liu, X.; Ma, C.; Wen, Y.; Chen, X.; Zhao, X.; Tang, T.; Holze, R.; Mijowska, E. Highly efficient conversion of waste plastic into thin carbon nanosheets for superior capacitive energy storage. *Carbon* **2021**, *171*, 819–828. [CrossRef]
31. Liu, T.; Zhang, F.; Song, Y.; Li, Y. Revitalizing carbon supercapacitor electrodes with hierarchical porous structures. *J. Mater. Chem. A* **2017**, *5*, 17705–17733. [CrossRef]
32. Gao, Y.; Yue, Q.; Gao, B.; Li, A. Insight into activated carbon from different kinds of chemical activating agents: A review. *Sci. Total Environ.* **2020**, *746*, 141094. [CrossRef] [PubMed]
33. Okabe, J.; Fang, Y.; Moriguchi, I.; Furó, I. Structural evolution by heat treatment of soft and hard carbons as Li storage materials: A joint NMR/XRD/TEM/Raman study. *J. Mater. Chem. A* **2025**, *13*, 13962–13975. [CrossRef]
34. Ferrari, A.C.; Basko, D.M. Raman spectroscopy as a versatile tool for studying the properties of graphene. *Nat. Nanotechnol.* **2013**, *8*, 235–246. [CrossRef] [PubMed]
35. Ferrari, A.C. Raman spectroscopy of graphene and graphite: Disorder, electron–phonon coupling, doping and nonadiabatic effects. *Solid State Commun.* **2007**, *143*, 47–57. [CrossRef]
36. Puziy, A.M.; Poddubnaya, O.I.; Socha, R.P.; Gurgul, J.; Wisniewski, M. XPS and NMR studies of phosphoric acid activated carbons. *Carbon* **2008**, *46*, 2113–2123. [CrossRef]
37. Major, G.H.; Fairley, N.; Sherwood, P.M.A.; Linford, M.R.; Terry, J.; Fernandez, V.; Artyushkova, K. Practical guide for curve fitting in x-ray photoelectron spectroscopy. *J. Vac. Sci. Technol. A* **2020**, *38*, 061203. [CrossRef]
38. Liu, X.; He, C.; Yu, X.; Bai, Y.; Ye, L.; Wang, B.; Zhang, L. Net-like porous activated carbon materials from shrimp shell by solution-processed carbonization and H3PO4 activation for methylene blue adsorption. *Powder Technol.* **2018**, *326*, 181–189. [CrossRef]
39. Qiu, C.; Jiang, L.; Gao, Y.; Sheng, L. Effects of oxygen-containing functional groups on carbon materials in supercapacitors: A review. *Mater. Des.* **2023**, *230*, 111952. [CrossRef]
40. Kiciński, W.; Szala, M.; Bystrzejewski, M. Sulfur-doped porous carbons: Synthesis and applications. *Carbon* **2014**, *68*, 1–32. [CrossRef]
41. Guan, X.; Li, X.; Wang, L.; Zhao, X.; Wang, Z.; Zhang, L.; Ma, J. Hierarchical porous sulfur self-doped lignin carbon derived from full component utilization of black liquor for high-performance supercapacitors. *Int. J. Biol. Macromol.* **2024**, *283*, 137703. [CrossRef] [PubMed]
42. Zhou, J.; Xu, L.; Li, L.; Li, X. Polytetrafluoroethylene-assisted N/F co-doped hierarchically porous carbon as a high performance electrode for supercapacitors. *J. Colloid Interface Sci.* **2019**, *545*, 25–34. [CrossRef] [PubMed]
43. Beguin, F.; Presser, V.; Balducci, A.; Frackowiak, E. Carbons and electrolytes for advanced supercapacitors. *Adv. Mater.* **2014**, *26*, 2219–2251. [CrossRef] [PubMed]
44. Dai, J.; Li, J.; Wang, K.; Li, J.; Tong, X.; Guo, D.; Zhao, H. Electrospinning fabrication of ethanol lignin/polyacrylonitrile composite carbon fibers for supercapacitor applications. *Int. J. Biol. Macromol.* **2025**, *322*, 146743. [CrossRef] [PubMed]
45. Ding, Z.; Lei, T.; Dong, L.; Pan, C.; Wang, R.; Pang, G.; Ren, S. Preparation and electrochemical properties of porous carbon derived from lignin. *Biomass Bioenergy* **2025**, *194*, 107688. [CrossRef]

46. Fan, D.; Fu, F.; Qiu, S.; Zhang, W.; Li, Z.; Huang, J. Optimizing the mesopore ratio of lignin-derived hierarchical porous carbon via etching and exfoliation towards high-performance supercapacitors. *Chem. Eng. Sci.* **2026**, *319*, 122222. [CrossRef]
47. He, M.; Wang, H.; Yang, J.; Chu, F.; Wu, Y.; Xiong, F. Development of high-performance flexible electrodes from lignin-derived carbon nanospheres and reduced graphene oxide for supercapacitors. *Colloids Surf. A Physicochem. Eng. Asp.* **2025**, *720*, 137160. [CrossRef]
48. Jiang, C.; Wu, W.; Tang, J.; Zhang, H.; Gan, C.; Zhou, Z. Lignin's leap to energy: Recycling fiberboard waste into high-efficiency supercapacitor electrodes. *Ind. Crops Prod.* **2025**, *225*, 120591. [CrossRef]
49. Jiang, C.; Zhang, H.; Wu, W. Lignin based regenerated cellulose guided supramolecular reassembly from waste MDF into nitrogen-doped hierarchical carbons for sustainable energy storage. *Bioresour. Technol.* **2026**, *444*, 133992. [CrossRef] [PubMed]
50. Li, J.; Guo, D.; Wang, Q.; Chen, X.; Li, J.; Sha, L.; Tong, X. Effective approaches to co-dope lignin based concave shaped carbon nanofibers with multiple elements for supercapacitors. *Int. J. Biol. Macromol.* **2025**, *307*, 141921. [CrossRef]
51. Lu, F.; Xu, J.; Li, Z.; Wang, X.; Zhou, J.; Wang, Y.; Tan, F. Self-synthesized carbon nanotubes exhibiting temperature-responsive effects to "modify" honeycomb lignin-based carbon aerogels for supercapacitor applications. *J. Energy Storage* **2025**, *110*, 115348. [CrossRef]
52. Ma, C.-Y.; Sun, Q.; Xu, L.-H.; Zhang, H.; Wen, J.-L.; Yang, S.; Liu, X.; Yuan, T.-Q. Unveiling the heterogeneous structure of native lignin in bamboo cell walls via a novel isolation method for high-value applications. *Green Chem.* **2026**, *28*, 5286–5299. [CrossRef]
53. Niu, X.; Bai, L.; Xu, X.; Xue, Y.; Chen, Z.; Wang, F. Hierarchically porous carbon derived from a sol-shaping strategy enabled by lignin-Fe3+ coordination for supercapacitors. *J. Electroanal. Chem.* **2026**, *1006*, 119874. [CrossRef]
54. Pan, H.; Yan, Y.; Jiang, D.; Song, X.; Li, R.; Wu, Y. Toward high-performance supercapacitors: Electrodes from solvent-fractionated lignin with enhanced activity. *Int. J. Biol. Macromol.* **2026**, *347*, 150773. [CrossRef] [PubMed]
55. Wang, X.; Liu, Z.; Lu, X.; Wang, T.; Wang, X.; Ma, S.; Hu, R. Deoxygenated lignin carbon aerogel with enhanced electrochemical performance in organic systems for supercapacitor applications. *Int. J. Biol. Macromol.* **2025**, *308*, 142412. [CrossRef] [PubMed]
56. Wang, Y.; Wu, S.; Chang, S.; Rong, K.; Dong, S. Lignin-Derived Hierarchically Porous Carbon Nanofibers via Deep Eutectic Solvent Electrospinning and Silica-Templated Etching for High-Performance Supercapacitors. *ACS Appl. Mater. Interfaces* **2025**, *17*, 44825–44839. [CrossRef] [PubMed]
57. Wei, X.; Bai, Q.; Zhu, P.; Ma, J.; Wang, Y.; Li, C.; Shen, Y.; Uyama, H. A bidirectional strategy of pore-creating and surface modification towards lignin-based carbon aerogels for enhanced energy storage. *Sustain. Mater. Technol.* **2025**, *45*, e01617. [CrossRef]
58. Ye, Y.; Deng, Y.; Bai, Y.; Shu, R.; Yin, T.; Tian, Z.; Guo, J.; Wang, C. Facile and sustainable preparation of lignin activated carbon for high performance supercapacitors. *Biomass Bioenergy* **2026**, *205*, 108584. [CrossRef]
59. Yin, Y.; Wu, S. Transforming kraft lignin into supercapacitor electrodes via graphene oxide assisted co-pyrolysis and activation. *Ind. Crops Prod.* **2025**, *237*, 122229. [CrossRef]
60. Zhang, J.; Feng, Z.; Wang, S.; Cao, Z.; Qi, X.; Wang, B.; Xin, M.; Tang, J. Enhancing electrochemical performance of lignin-based carbon fibrous aerogels via boron doping. *Int. J. Biol. Macromol.* **2025**, *295*, 139639. [CrossRef] [PubMed]
61. Zhao, X.; Wang, X.; Gao, P.; Zhao, P.; Wang, J.; Li, Y.; Han, Z.; Shen, B. Eco-friendly synthesis coupled with predictive analytics: Developing hierarchical lignin-derived ordered mesoporous carbon for advanced supercapacitors. *Green Energy Environ.* **2025**, *10*, 1256–1269. [CrossRef]
62. Song, Z.; Miao, L.; Ruhlmann, L.; Lv, Y.; Zhu, D.; Li, L.; Gan, L.; Liu, M. Self-Assembled Carbon Superstructures Achieving Ultra-Stable and Fast Proton-Coupled Charge Storage Kinetics. *Adv. Mater.* **2021**, *33*, e2104148. [CrossRef] [PubMed]
63. Liu, M.; Li, X.; Shao, C.; Han, C.; Liu, Y.; Li, X.; Ma, X.; Chen, F.; Liu, Y. Synchronous-ultrahigh conductive-reactive N-atoms doping strategy of carbon nanofibers networks for high-performance flexible energy storage. *Energy Storage Mater.* **2022**, *44*, 250–262. [CrossRef]
64. Zhang, X.; Wang, X.; Jiang, L.; Wu, H.; Wu, C.; Su, J. Effect of aqueous electrolytes on the electrochemical behaviors of supercapacitors based on hierarchically porous carbons. *J. Power Sources* **2012**, *216*, 290–296. [CrossRef]
65. Suss, M.E.; Baumann, T.F.; Worsley, M.A.; Rose, K.A.; Jaramillo, T.F.; Stadermann, M.; Santiago, J.G. Impedance-based study of capacitive porous carbon electrodes with hierarchical and bimodal porosity. *J. Power Sources* **2013**, *241*, 266–273. [CrossRef]
66. Lu, Q.; Zhou, T.; Chen, M.; Sun, H.; Liu, Q. Water decomposition side reactions in aqueous supercapacitors. *Coord. Chem. Rev.* **2026**, *550*, 217389. [CrossRef]
67. Wang, Y.; Song, Y.; Xia, Y. Electrochemical capacitors: Mechanism, materials, systems, characterization and applications. *Chem. Soc. Rev.* **2016**, *45*, 5925–5950. [CrossRef] [PubMed]
68. Chomkhuntod, P.; Iamprasertkun, P.; Chiochan, P.; Suktha, P.; Sawangphruk, M. Scalable 18,650 aqueous-based supercapacitors using hydrophobicity concept of anti-corrosion graphite passivation layer. *Sci. Rep.* **2021**, *11*, 13082. [CrossRef] [PubMed]
69. Zheng, F.; Li, Y.; Wang, X. Study on effects of applied current and voltage on the ageing of supercapacitors. *Electrochim. Acta* **2018**, *276*, 343–351. [CrossRef]

70. Ding, Z.; Wang, R.; Pang, G.; Dong, L.; Lei, T.; Ren, S. Exploring the Connection Between the Structure and Activity of Lignin-Derived Porous Carbon Across Various Electrolytic Environments. *Molecules* **2025**, *30*, 494. [CrossRef] [PubMed]
71. Guan, X.; Zhang, L.; Li, X.; Lu, H.; Wang, Z.; Ma, J.; Ni, Y. Design of lignin-derived elastic gradient-pore biocarbon with enhanced interfacial effects for supercapacitor applications. *Chem. Eng. J.* **2026**, *528*, 172270. [CrossRef]
72. Hui, W.; Wang, X.; Hu, Z.-L.; Zhao, M.-Y.; Feng, J.-X.; Chen, W.; Xiao, X.-Y.; Zheng, C.-Q.; Pu, L. Waste lignin-based N/O-rich carbon nanofibers as bifunctional materials for efficient CO2 conversion and energy storage. *J. Environ. Chem. Eng.* **2026**, *14*, 121336. [CrossRef]
73. Moagi, V.M.; Maphoru, M.V.; Mabena, L.F. Preparation, characterisation, and electrochemical evaluation of nickel sulphide on lignin-derived carbon material for supercapacitors. *Electrochim. Acta* **2025**, *540*, 147019. [CrossRef]

Disclaimer/Publisher's Note: The statements, opinions and data contained in all publications are solely those of the individual author(s) and contributor(s) and not of MDPI and/or the editor(s). MDPI and/or the editor(s) disclaim responsibility for any injury to people or property resulting from any ideas, methods, instructions or products referred to in the content.